ACS OMEGA

http://pubs.acs.org/journal/acsodf

Article

Multifunctional CdS Nanoparticle-Decorated CeO_2 as Efficient Visible Light Photocatalysts and Toxic Cr(VI) Sensors

Lisamoni Kalita, Karanika Sonowal, Purashri Basyach, Biswajit Saha, and Lakshi Saikia*

Cite This: *ACS Omega* 2023, 8, 11768−11781

Read Online

ACCESS | Metrics & More | Article Recommendations | Supporting Information

ABSTRACT: Several one-dimensional and three-dimensional CdS@CeO_2 nanocomposites were synthesized by a solvothermal route. A nanoflower-shaped CdS@CeO_2 nanocomposite (CdS-NF@CeO_2) was selected as the model catalyst after various characterizations. It was, then, employed directly as a luminescent sensor for Cr(VI) detection in an aqueous medium. A good linear quenching was observed in the range of 0−0.5 μM with a detection limit of 0.04 μM. The quantum yield of the catalyst was found to be 73%. Moreover, our catalyst is highly selective toward Cr(VI) and can be applied as an efficient sensor for real water analysis. The efficiency of the catalyst was also tested in controlling the photocatalytic activity for oxidation of benzylamine to N-benzylidenebenzylamine under a domestic LED bulb with molecular O_2 as a sole, green oxidant. Conversion (>99.9%) and selectivity as high as 100% were observed for the CdS-NF@CeO_2 photocatalyst. These results show the potential applications of CdS-NF@CeO_2 nanocomposites as an efficient photocatalyst for organic transformation and environmental remediation.

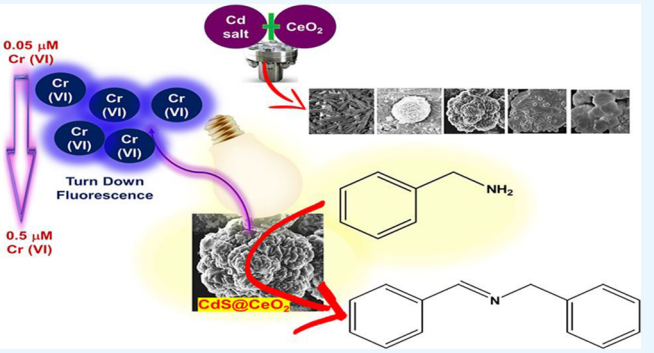

1. INTRODUCTION

With the rapid consumption of nonrenewable fossil fuels leading to energy shortage, the development of renewable clean energy production for a sustainable human society establishment has garnered immense attention in the 21st century.[1−4] Considerable effort has been made toward efficiently harvesting solar energy, which is abundantly available, green in nature, sustainable, cost-effective, and a viable energy source.[5] Conversion of solar energy to chemical energy via photocatalysis is an economically efficient, environmentally friendly, and durable technology that relies on the employment of semiconductor photocatalysts for harvesting light of the solar spectrum to trigger chemical transformations.[6−9]

CdS, a classical II−VI semiconductor, is one of the most vital visible light photocatalysts owing to its narrow bandgap of 2.4 eV, which corresponds to the solar spectrum. This excellent property of CdS led to its wide applications in several fields viz. electrical, optical, light-emitting diodes (LEDs), lasers, solar cells, and dye degradation, to name a few.[10,11] Considering the fact that the properties of semiconductor nanomaterials largely depend on their size and shape, altering the morphologies results in interesting novel characteristics of the materials leading them to find enormous applications.[12−15] Voluminous research has been undertaken to synthesize several 1-D and 3-D CdS nanostructures such as nanorods, nanowires, nanotubes, dendritic, nanotrees, sea-urchin shaped ones, etc. via a solvothermal route.[4,16−20] Chen et al. synthesized various morphologies of CdS crystals using a hydrothermal process and performed an in-detail analysis of the formation mechanism.[13] However, the influence of different CdS morphologies on organic transformation reactions has been rarely investigated. Despite its intriguing properties, pure CdS suffers from the drawback of rapid recombination of photogenerated electron−hole pairs and photocorrosion. To overcome this downside, researchers have devoted numerous efforts by combining CdS with other materials having suitable band structures. Previous reports have been particularly based on the coupling of CdS with other transition metal oxides, such as ZnO, TiO_2, Fe_2O_3, etc. For instance, Yang et al. fabricated CdS/ZnO nanoheterojunctions to prevent photocorrosion and diminish the recombination rate while employing them for photocatalytic solar water splitting.[21] Liu and co-workers synthesized 1-D CdS@TiO_2 core−shell nanocomposites for evaluating the selective oxidation−reduction efficiency under visible light irradiation.[9] Little effort has been concentrated on integrating CdS with rare-earth oxide, cerium dioxide (CeO_2). Among the various photocatalysts, $CeO_2$with a wide bandgap

Received: September 7, 2022
Accepted: March 13, 2023
Published: March 23, 2023

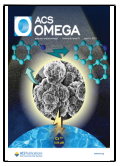

of 3.2 eV is an emerging material, which is highly stable, nontoxic, inexpensive, and benign to the environment yet it is active only under ultraviolet (UV) light, restricting its application in the visible light region.[22,23] Hence, to overcome this constraint and enhance the light-harvesting potentiality of CeO_2, ion or metal doping and construction of heterojunctions were usually employed.[24−26] Theoretically, matched band structures of CdS and CeO_2 enable their coupling, which would provide a practical strategy to investigate the visible-light-harvesting performance of the composites.[27]

Even though chromium (Cr) is an essential trace element in humans, numerous anthropogenic activities mainly in the industrial fields, such as coal burning, leather tanning, metal smelting, etc. have led to the contamination of chromium in groundwater.[28] Cr(VI) is a highly toxic bioaccumulant, and being a carcinogen, it can damage DNA even at ultratrace levels.[29] According to World Health Organization (WHO) guidelines, the maximum contaminant level of Cr(VI) in drinking water is 50 μg/L.[30] Hence, the detection of Cr(VI) at the lowest amount possible has become hugely indispensable. Costly techniques that are used traditionally for Cr(VI) detection such as inductively coupled plasma-mass spectroscopy and atomic absorption spectroscopy can be circumvented by the use of a fluorometric technique tht is highly sensitive and simple, as well as cost-effective and time efficient.

Selective oxidation of amines to imines is, in particular, a fundamental yet significant chemical transformation because imines have extensive applications in the production of medicines and heterocyclic chemicals.[31−33] Very recently, Bai et al. reported the oxidative coupling of benzylamine to its corresponding imine using a $Bi_2O_2CO_3$ photocatalyst. While they achieved >99% selectivity, high oxygen pressure (0.3 MPa) and unreasonable Xe lamps were necessary to their reaction system.[5] Mon and co-workers reported the imination of primary alcohols using very expensive Ru-catalysts.[34] Among all the methodologies for imine synthesis, oxidation of secondary amine to imine,[35] alcohol, and amine coupling,[36] and other approaches,[37,38] the photocatalytic dimerization of primary amine using a simple, cost-effective process utilizing molecular oxygen as the sole oxidant under ambient conditions is highly desirable from a green chemistry view.

Considering the advantage of CdS@CeO_2 as a photocatalyst, the nanocomposites were synthesized via a simple one-step solvothermal method free from any additional surfactant or capping agent and by varying the solvent and temperature. The as-synthesized materials were employed in the visible-light-assisted highly selective oxidative coupling of amines to imines in the presence of molecular oxygen and for the detection of Cr(VI) in water. To the best of our knowledge, synthesis of CdS@CeO_2 nanocomposites with varied morphologies including rods, dandelions, spheres, and flowers and applications in the photocatalytic study of the oxidation of benzylamine as well as a fluorescent sensor for Cr(VI) detection have been reported for the first time. In the detection of Cr(VI), a good linear relationship between the concentration of Cr(VI) ions and the photoluminescence (PL) quenching efficiency of the flower-like CdS@CeO_2 nanocomposite was obtained in the ranges from 0.05 to 0.5 μM (R^2 = 0.9853), and the limit of detection (LOD = 3σ/S) was calculated as 0.04 μM. It was also observed that the flower-like CdS@CeO_2 showed the highest photocatalytic activity with as high as >99.9% conversion and 100% selectivity to N-benzylidenebenzylamine. The use of molecular O_2 as the sole oxidant, ambient reaction conditions, high atom economy, absence of additives such as acid or base, green energy source, no side product, and high conversion and selectivity make the process advantageous over other studies. We also report the mechanistic pathways and kinetic analysis of the oxidation reaction comprehensively. Moreover, the recycling experiments revealed the highly stable nature of the catalysts until the fifth catalytic run.

2. EXPERIMENTAL DETAILS

2.1. Ceria (CeO_2) Synthesis. CeO_2 was synthesized by taking the required amount of $Ce(NO_3)_3.6H_2O$ in a silica crucible and maintained at 350 °C for 2 h in a muffle furnace. The resulting creamy-white powder was collected, ground, and kept for further use.

2.2. Synthesis of Cadmium Disulfide (CdS) and CeO_2 Nanocomposites.

a. CdS nanorods (CdS-NR) were synthesized by a solvothermal method. In a typical process, 1.5 M $CdCl_2$ and 3 M CH_4N_2S were added to 30 mL of ethylenediamine with continuous stirring at room temperature for 6 h, transferred to a 100 mL autoclave, and filled to 80% of the total volume. Yellow precipitates were obtained after maintaining the temperature at 180 °C for 24 h. Finally, the precipitates were filtered, washed, and dried at 60 °C for 13 h.

10 wt % CdS@CeO_2(10% CdS-NR@CeO_2) was prepared by first sonicating 50 mg of CdS-NR and 500 mg of CeO_2in 100 mL distilled water for 30 min. The suspension was, then, stirred strenuously for 12 h at room temperature before evaporating the solvent in a rotavapor and consequently drying them at 60 °C for 12 h.

b. Flower-shaped CdS@CeO_2 (CdS-NF@CeO_2) was synthesized by a similar solvothermal technique by using 50 mL absolute ethanol +30 mL water as the solvent and a temperature of 180 °C. All other measurements remained unchanged as in CdS-NR. In a similar technique, CdS nanoflowers (CdS-NF) were prepared without adding CeO_2.
c. Nanodandelion CdS@CeO_2 (CdS-HF@CeO_2) synthesis was similar to the flower-shaped one, which was obtained by replacing distilled water with ethanol and temperature to 110 °C and unvarying all other parameters.
d. In a similar technique to (c), flat spherical flower-like CdS@CeO_2 (CdS-RL@CeO_2) was synthesized by just changing the temperature to 130 °C and keeping other conditions constant.
e. Another CdS@CeO_2 with irregular morphology (CdS-S@CeO_2) was obtained by ethylene glycol as a solvent and a temperature of 150 °C, other parameters remained unchanged as (d).

2.3. Procedure for Fluorescence Sensing of Cr(VI) in Water. The CdS-NF@CeO_2 suspension (5 mg/ mL) in distilled water was prepared and employed directly as a fluorescent sensor for Cr(VI) detection. A series of Cr(VI) solutions were prepared (0−0.5 μM), and the fluorescence (FL) intensities were recorded and evaluated by (F_0− F)/F_0, where F_0 and F are the FL intensities in the absence and presence of the target ion, respectively. To acquire the calibration curve, different concentrations of Cr(VI) (0.05−0.5 μM) were obtained. The selectivity of the sensor was

https://doi.org/10.1021/acsomega.2c05811
ACS Omega 2023, 8, 11768−11781

assessed by recording the FL intensities of CdS-NF@CeO_2 suspension (5 mg/ mL) in water containing 0.25 μM metal ions (Cr^{3+}, Hg^{2+}, Fe^{3+}, Cu^{2+}, Ni^{2+}, Pb^{2+}, Mn^{2+}, Ag^{+}, Al^{3+}, As^{5+}, Fe^{2+}, Au^{3+}, Zn^{2+}, and Co^{2+}) or anions (F^{-}, Cl^{-}, Br^{-}, I^{-}, CO_3^{2-}, PO_4^{3-}, SCN^{-}, SO_4^{2-}, and MnO_4^{-}). The recovery of the sensor was obtained by recording FL intensities of CdS-NF/CeO_2 tap-water and groundwater suspensions (5 mg/ mL) containing 0.05, 0.25, and 0.5 μM Cr(VI). All the samples were excited at 330 nm, and the FL emission was recorded at 418 nm.

2.4. Procedure for Photocatalytic Oxidative Coupling of Amines. 1 mmol of amine, 10 mg of catalyst, and 1.5 mL of 1,4-dioxane were added into a 10 mL round-bottomed flask and stirred in the dark for 30 min. The mixture was, then, purged with O_2 gas and finally connected with an O_2-balloon. It was irradiated with four domestic LED bulbs (9 W each) having an intensity of 806 candela at room temperature and magnetically stirred at 900 rpm. At certain time intervals, an aliquot of the reaction mixture was taken and analyzed by gas chromatography, GC (Thermo Scientific, TRACE 1300). The conversion of amine and yield of imine were calculated as:

$$\text{conversion } (\%) = [(C_a - C_t)/C_o] \times 100$$

$$\text{yield } (\%) = [C_i/C_a] \times 100$$

where C_a, C_t, and C_i denote the initial amine concentration, the concentration of amine at the time "t", and the imine concentration, respectively. The progress of the reaction was inspected by thin-layer chromatography as well as GC. On completion of the reaction, the catalyst was centrifuged, washed several times with ethanol, and dried overnight in a vacuum desiccator for further characterization and successive reactions.

3. RESULTS AND DISCUSSION

3.1. Structural Characterization. The crystallographic properties of CdS@CeO_2 nanocomposites are depicted in the powder X-ray diffraction (PXRD) patterns (Figure 1) where the intense peaks reveal the high crystallinity of the materials.

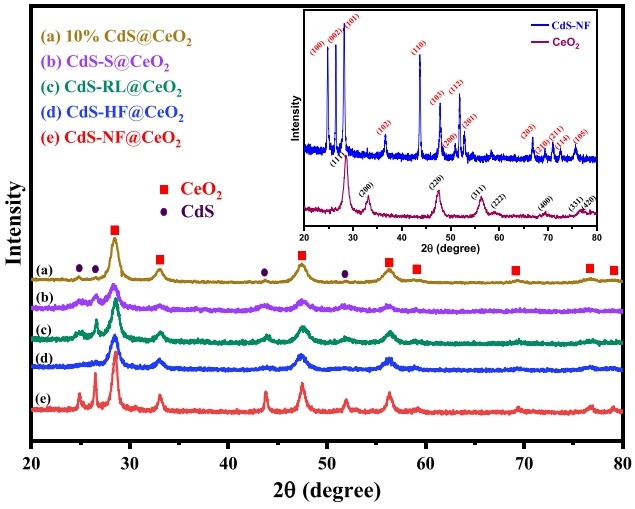

Figure 1. PXRD patterns of all the as-synthesized CdS@CeO_2 nanocomposites, (a) 10% CdS@CeO_2, (b) CdS-S@CeO_2, (c) CdS-RL@CeO_2, (d) CdS-HF@CeO_2, and (e) CdS-NF@CeO_2. The inset shows the PXRD patterns and crystal planes of bare CeO_2 and CdS-NF.

The inset shows the XRD pattern of CeO_2 and CdS-NR. The peaks of CeO_2 and CdS-NR are assigned to the cubic (JCPDS Card No. 81-0792) and hexagonal (JCPDS Card No. 75-1545) phases, respectively. In addition, the XRD patterns of synthesized CdS@CeO_2 nanocomposites also matched with CdS hexagonal structure. The high purity of the samples is ascertained by the nonappearance of any diffraction peaks, such as at 31.5° for the cubic blende phase of CdS.[12] Peaks for both CdS and CeO_2were present in the diffractograms, which obviously indicates the effective formation of CdS@CeO_2 composites. However, the characteristic (111) peak of CeO_2 at 28.4° overlapped with the (101) peak of CdS. The crystallite sizes for CdS@CeO_2 nanocomposites considering the (002) plane calculated by employing Scherrer's equation evidently specify the formation of nanocrystals and are reported in Table 1. Table 1 also reports the BET surface area, pore volume, and

Table 1. Results of Crystallite Size, BET Surface Area, Pore Volume, and Pore Radius of CdS@CeO_2 Nanocomposites

CdS@CeO_2 samples	crystallite size (nm)	BET surface area (m^2g^{-1})	pore volume (cm^3g^{-1})	pore radius (nm)
10% CdS-NR@CeO_2	27.9	67.3	0.35	6.2
CdS-NF@CeO_2	26.7	128.5	0.13	1.8
CdS-HF@CeO_2	9.4	231.8	0.35	1.8
CdS-RL@CeO_2	23.8	130.2	0.23	1.9
CdS-S@CeO_2	8.7	34.2	0.08	8.4
CeO_2	7.6	75.3	0.03	40.5
CdS-NR	44.2	20.4	0.11	1.9

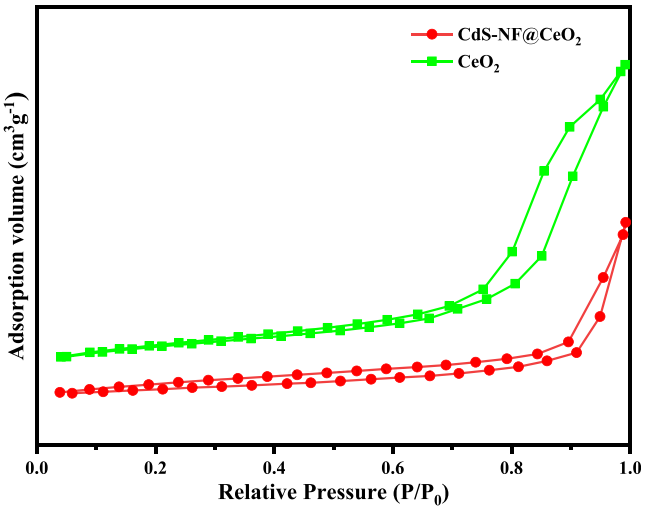

Figure 2. N_2-sorption isotherm of CdS-NF@CeO_2 nanocomposite and bare CeO_2.

pore radius of the materials. From Figure 2 it is observed that the synthesized CdS-NF@CeO_2 nanocomposite is porous in nature indicated by the type IV isotherms, and the mesoporosity can be established from the H3 hysteresis loop according to IUPAC classification. The specific surface area and pore volume of CdS-NF@CeO_2 increased in comparison to CeO_2 (75.3 m^2g^{-1} and 0.031 cm^3g^{-1}). This illustrates that CdS-NFs were effectively dispersed over the CeO_2 surface resulting in new pores. Furthermore, no noteworthy change is

https://doi.org/10.1021/acsomega.2c05811
ACS Omega 2023, 8, 11768−11781

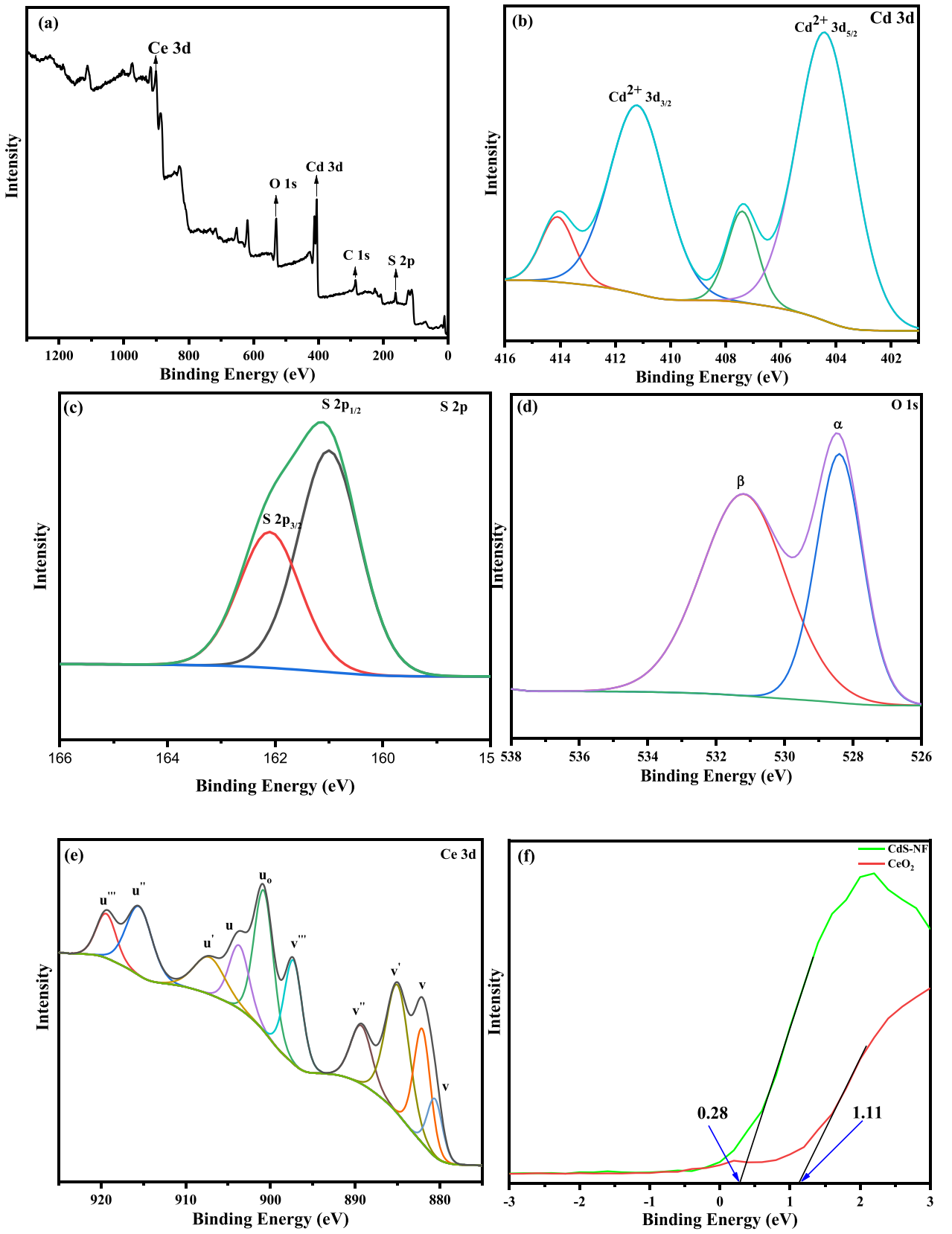

Figure 3. XPS spectra of CdS-NF@CeO_2 nanocomposites, (a) Survey spectra, (b) Cd 3d, (c) S 2p, (d) O 1 s, (e) Ce 3d, and (f) valence-band spectra of CdS-NF and CeO_2.

observed in the phase structure of CdS-NF@CeO_2 (Figure S1) confirming the stability and intact crystal structure of the material even after the catalytic process. Then again, the synthesized CdS@CeO_2 nanocomposites are found to exhibit higher surface areas than most of the reported ones (Table S1). Typical peaks for Ce−O stretching at 539, 892, and 1117

https://doi.org/10.1021/acsomega.2c05811
ACS Omega 2023, 8, 11768−11781

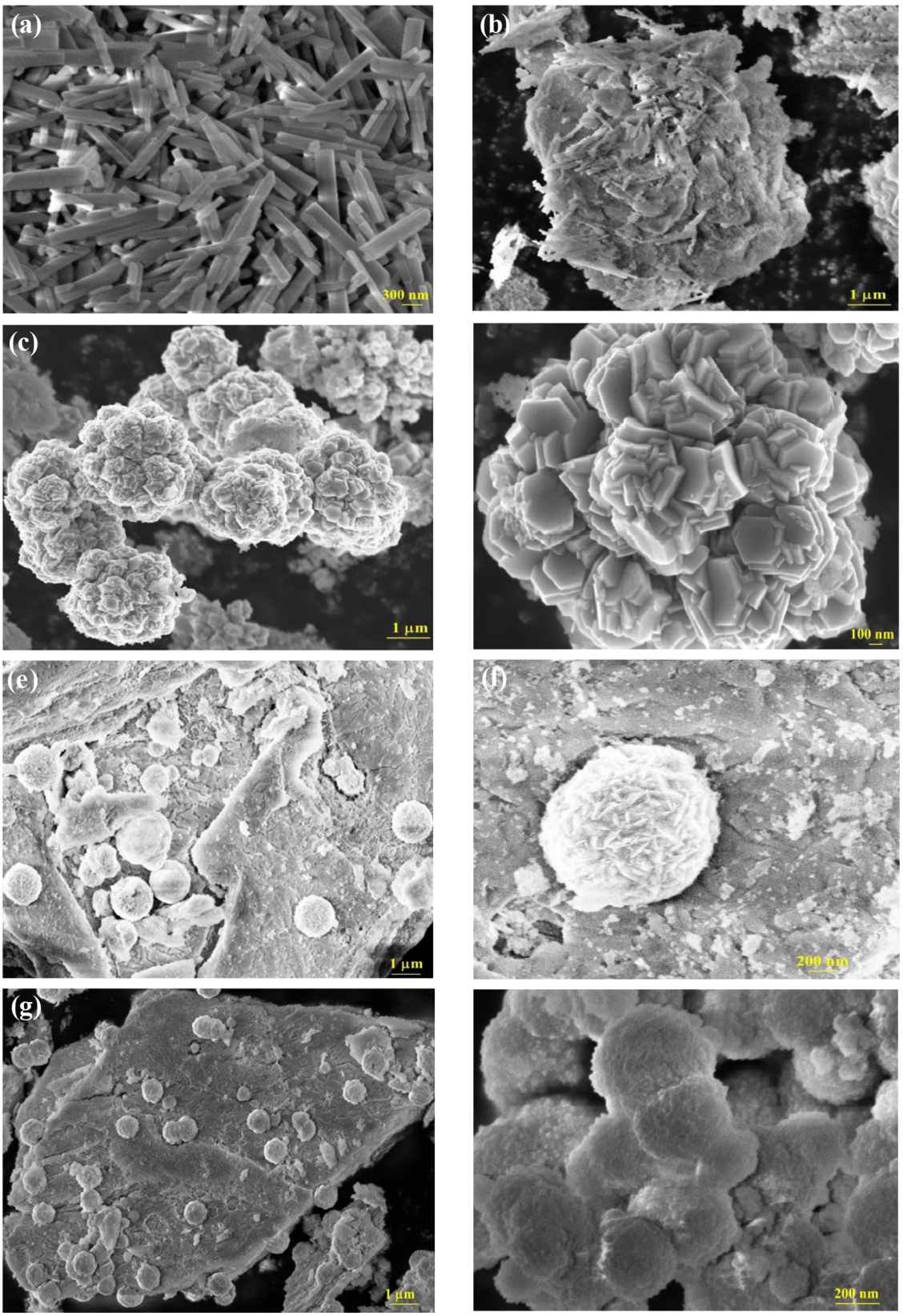

Figure 4. FESEM images of (a) CdS-NR, (b) 10% CdS-NR@CeO_2, (c, d) CdS-NF@CeO_2, (e, f) CdS-HF@CeO_2, (g) CdS-RL@CeO_2, and (h) CdS-S@CeO_2 nanocomposites.

cm^{-1} for Cd-S bond and S−H stretching band at 2340 cm^{-1} are observed in the FTIR spectra of CdS-NF@CeO_2 (Figure S2).[39,40]

Evaluation of surface chemical composition and chemical states of the synthesized CdS@CeO_2 nanocomposites were done via the X-ray photoelectron spectroscopy (XPS)

https://doi.org/10.1021/acsomega.2c05811
ACS Omega 2023, 8, 11768−11781

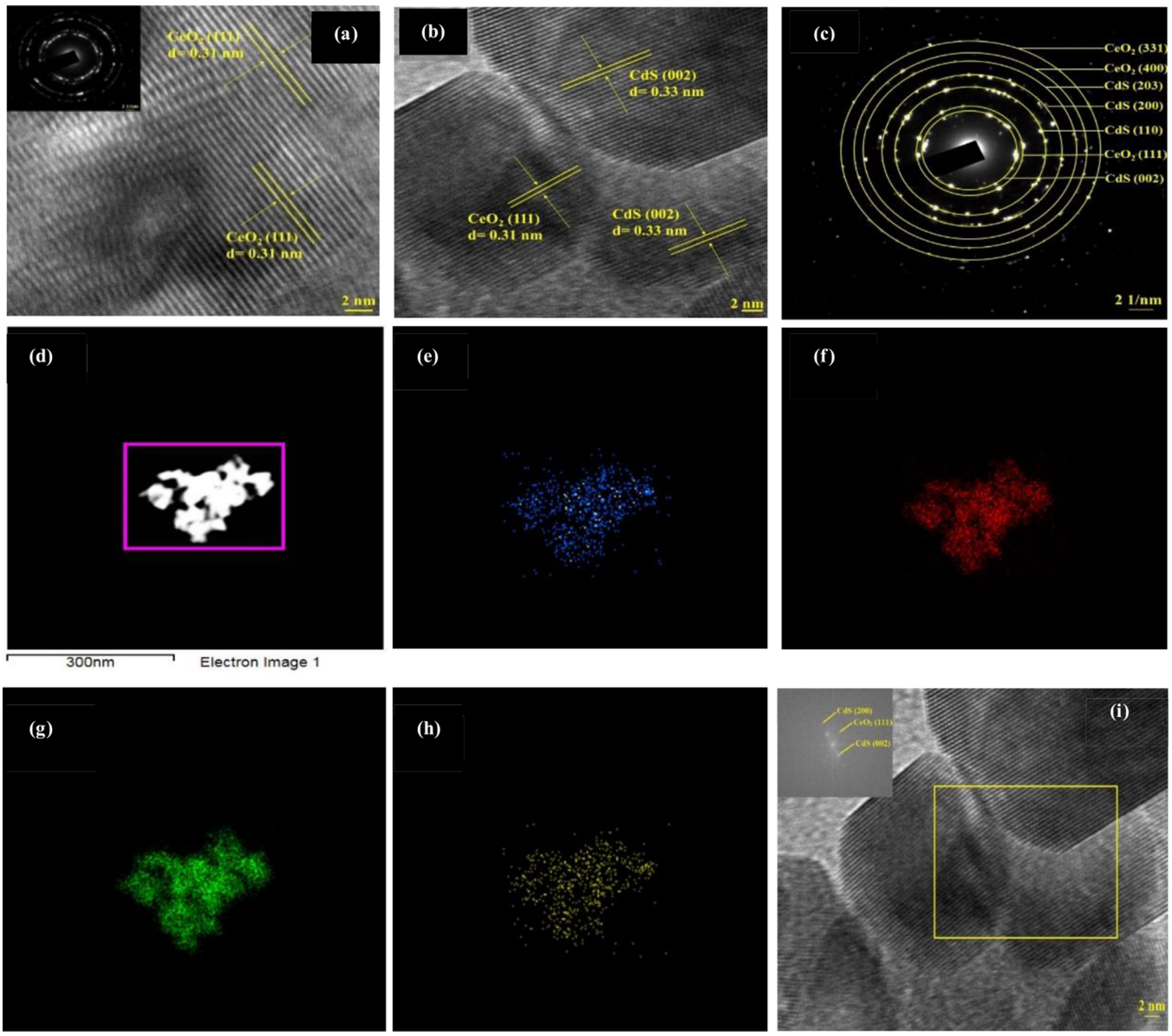

Figure 5. HRTEM images of (a) CeO_2, inset shows the SAED pattern of (b) CdS-NF@CeO_2, (c) SAED pattern of CdS-NF@CeO_2, (d) HAADF-STEM image of CdS-NF@CeO_2, (e-h) elemental mapping of CdS-NF@CeO_2, and (i) FFT of CdS-NF@CeO_2.

technique. Figure 3a−e represents the XPS survey of the CdS-NF@CeO_2 composite. As can be seen in Figure 3a, the typical peaks of Cd, S, Ce, O, and C are detected, confirming the successful composite formation of CdS and CeO_2. The C impurity may result possibly due to adventitious carbon as a reference. The peaks present at 404.4 and 411.2 eV correlate to $3d_{5/2}$ and $3d_{3/2}$ of Cd^{2+} respectively (Figure 3b), wherein the spin-orbit separation of 6.8 eV is representative of the Cd^{2+} state.[41] Satellite peaks of $Cd^{2+}$are visible at 407.4 and 414.1 eV. The S 2p spectra (Figure 3c) exhibit peaks at 161.0 and 162.1 eV with an energy splitting of 1.1 eV imputed to the S^{2-} state of CdS. The presence of lattice oxygen (O_α) and oxygen vacancies (O_β) can be substantiated by the binding energy peaks at 528.4 and 531.2 eV respectively (Figure 3d). Moreover, Burroughs labels are used to identify the XPS peaks of Ce 3d spectrum, where "v" and "u" implies the spin-orbit coupling $3d_{5/2}$ and $3d_{3/2}$.[39] Figure 3e shows ten peaks for Ce 3d core, which can be grouped accordingly: five components assigned to $3d_{5/2}$ as v_o (880.7 eV), v(882.2 eV), v' (885.2 eV), v'' (889.4 eV), and v''' (897.4 eV), and five features of $3d_{3/2}$ as u_o (900.6 eV), u (903.8 eV), u' (907.3 eV), u'' (915.8 eV), and u''' (919.4 eV). The v_o, v, v', v'', and v''' can be designated to the Ce ($4f^2$) O ($2p^5$), Ce ($4f^2$) O ($2p^4$), Ce ($4f^1$) O ($2p^6$), Ce ($4f^1$) O ($2p^5$), and Ce ($4f^0$) O ($2p^6$), respectively. By similar means, the "u" structures can also be explained. Then again, v_o, v', u_o, u' are characteristic peaks of Ce^{3+} state and v, v'', v''', u, u', u''' are characteristics of Ce^{4+} state. Peaks at binding energies 907.1 and 886.7 eV are attributable to the satellite peaks (shake-up) corresponding to Ce^{3+} $3d_{3/2}$ and Ce^{3+} $3d_{5/2}$ states. A comparison of XPS spectra of all the CdS@CeO_2 nanocomposites is given in Figure S3a–d. The slight shifting of peaks for Cd 3d and S 2p visible in Figure S3a,b in the case of 10% CdS-NR@CeO_2 may be because of variation in the chemical environment. The valence-band edge (E_{VB}) of CeO_2 and CdS-NF were evaluated too by valence-band (VB) XPS (Figure 3f). The E_{VB} of CeO_2 and CdS-NF was 1.11 and 0.28 eV, respectively.

https://doi.org/10.1021/acsomega.2c05811
ACS Omega 2023, 8, 11768−11781

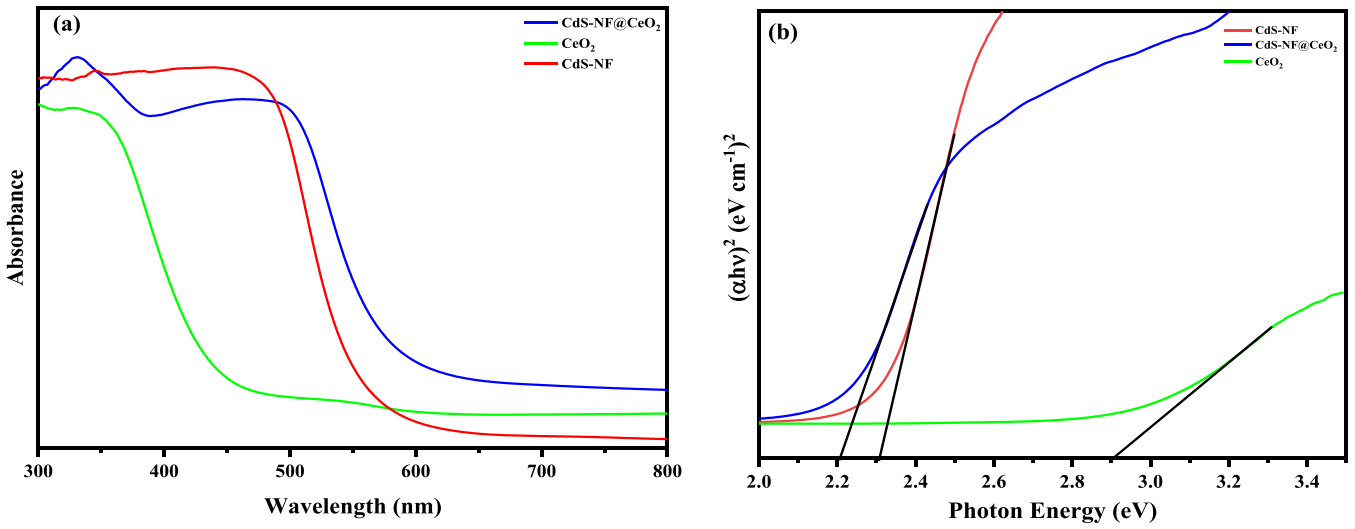

Figure 6. (a) UV−vis diffuse reflectance spectra and (b) Tauc plot of CeO_2, CdS-NF, and CdS-NF@CeO_2 nanocomposite.

The structural morphology of the synthesized CdS@CeO_2 nanocomposites was evaluated by field-emission scanning electron microscopy (FESEM) analysis (Figure 4). The SEM images verifies the formation of varied morphologies like nanorods (a, b), flower-shaped (c, d), dandelion-shaped (e, f), and spherical (g, h). The SEM analysis of blank CeO_2 was also conducted (Figure S4). The image reveals the surface of the as-synthesized CeO_2. Uniformly formed CdS nanorods (CdS-NR) with length (0.4−1.5 μm) and diameter (86−190 nm) are visible in Figure 4a when ethylenediamine was used as a solvent. The ethylenediamine forms a complex with Cd^{2+} and then gets adsorbed onto the CdS surface. With time, ethylenediamine dissociates from the surface to orient the formation of nanorods. The presence of CdS nanorods on the CeO_2 surface is clearly visible in Figure 4b upon loading 10 wt % of CdS-NR onto CeO_2. The role of water is the hydrolysis of Cd^{2+} and the formation of the precursor. The chelating behavior of thiourea controls the morphology in this case. Then again, on using a mixed solvent system of 60% alcohol and water, uniformly formed CdS-NF@CeO_2 nanoflowers with hexagonal petals can be seen (Figure 4c). Over time, several hexagonal petals stacked together to yield the nanoflowers. Again, some individual nanoflowers fused together to form larger aggregates (Figure 4d). The size of the nanoflowers ranged between (2−3 μm) with a diameter of 0.3 μm. Dandelion-shaped CdS-HF@CeO_2 are visible in Figure 4e,f. The CdS nanosheets assembled to form the dandelion-shaped CdS particles of size (around 1 μm) over the CeO_2 surface on changing the solvent to pure alcohol (absolute ethanol) system. Since the chelating behavior of thiourea is different in different solvents, hence this will lead to a change in surface energy and consequently result in varied morphologies. Likewise, on using the same ethanol system but changing the temperature to 130 °C, spherical CdS distributed over CeO_2surface (CdS-RL@CeO_2) were obtained (Figure 4g) with a diameter of 0.7 μm. This change may be due to the temperature rise and as a result, the dandelions collapsed to form flat spherical particles. Ethylene glycol as a solvent, also, resulted in spherical particles of diameter (0.2−0.5 μm) (Figure 4h). The strong chelating ability of ethylene glycol renders the dissolution of inorganic materials yielding uniform solutions. Its coordination with Cd^{2+} followed by nucleation with S^{2-} to finally grow into primary CdS crystals, which can assemble into 3D aggregates resulting in the corresponding structure. Thus, it can be said that the solvents and substrates act as structure-directing agents in our synthesis technique, which ruled out the need for additional templates. Although variation of temperature also resulted in the increase of size in the 3-D nanomaterials like CdS-S@CeO_2, CdS-RL@CeO_2, CdS-HF@CeO_2, CdS-NF@CeO_2 with increasing temperature from 110 to 180 °C, its role in morphology changes might be negligible considering the same temperature of 180 °C used in nanorods (CdS-NR) and CdS-NF@CeO_2 synthesis process. The stability of the morphology of CdS-NF@CeO_2 was also studied after storing for 1 year under ambient conditions. Figure S5 clearly shows that the catalyst morphology was intact even after a year. Energy-dispersive X-ray spectroscopy (EDS) analysis for CdS-NF@CeO_2gavethe elemental compositions (wt %) of Cd, S, Ce, and O to be 6.9, 2.1, 12.0, and 22.9, respectively and the EDS spectrum is provided in Figure S6.

To further confirm the formation of CdS-NF@CeO_2 nanocomposites, and evaluate the crystal facets HRTEM analysis was effectuated. The HRTEM image (Figure 5a) of bare CeO_2 reveals that the lattice plane (111) is repeatedly found in the nanostructure. The inset shows the selected area diffraction (SAED) pattern clearly depicting the polycrystalline nature of CeO_2. The elemental distributions in CeO_2 were evaluated by EDS elemental mapping (Figure S7). From Figure 5b, the existence of two crystalline phases and their interfaces having interplanar spacings of 0.31 and 0.33 nm indexed to the (111) and (002) crystal facets of cubic CeO_2 and hexagonal CdS respectively are evident. The polycrystalline nature of the nanocomposite was further confirmed by the SAED pattern (Figure 5c). The SAED pattern verifies the coexistence of the lattice planes of both CdS and CeO_2 in the nanocomposite, which complies with the XRD findings. The high-angle annular dark-field scanning transmission electron microscopy (HAADF-STEM) image for the CdS-NF@CeO_2 nanocomposite and the corresponding EDS elemental mapping distinctly demonstrate the homogeneous distribution of Cd and S over CeO_2 (Figure 5d−h). The inset in Figure 5i represents the FFT pattern observed for the marked area. The FFT pattern further confirms the presence of the characteristic (002), (200) planes of CdS, and (111) planes of CeO_2 with

https://doi.org/10.1021/acsomega.2c05811
ACS Omega 2023, 8, 11768−11781

Table 2. Optical Band Gap of the As-Synthesized Samples

sample	CeO_2	CdS-NF	CdS-NR	CdS-NF@CeO_2	CdS-HF@CeO_2	CdS-RL@CeO_2	CdS-S@CeO_2	10% CdS-NR@CeO_2
band gap (eV)	2.90	2.30	2.37	2.20	2.32	2.31	2.23	2.36

interplanar spacings 0.33, 0.17, and 0.31 nm, respectively. Thus, the TEM findings positively established the successful formation of the CdS-NF@CeO_2 nanocomposite.

UV−Vis diffuse reflectance spectroscopy (DRS) was employed for studying the optical properties of the nanocomposites (Figure 6a). The direct band gap energy was calculated by employing the Tauc plot ($\alpha h\nu$ vs $h\nu$), where α is the absorption coefficient and $h\nu$ is the photon energy (Figure 6b). Bare CeO_2 shows strong absorption in the UV region with an absorption edge at 450 nm due to the charge transfer transition from 2p to 4f orbitals of O(II) and Ce(IV), respectively. Owing to the narrow band gap (2.3 eV) of CdS-NF, a broad absorption is observed in a wavelength range starting from UV region to ∼560 nm. On the other hand, the nanocomposite CdS-NF@CeO_2 displays a bathochromic shift in the spectra (∼590 nm), which signifies the further lowering of the band gap and enhancement of visible light response. The CdS-NF@CeO_2 nanocomposite exhibits two absorption edges inferred to the successful merging of photoresponse properties of both CeO_2 and CdS-NF. The absorbance spectra and Tauc plot of all other composites are given in the Supplementary Information (Figure S8a,b). The optical band gap of the samples is listed in Table 2. PL was performed to analyze the photogenerated charge separation efficacy of CdS (Figure 7) at

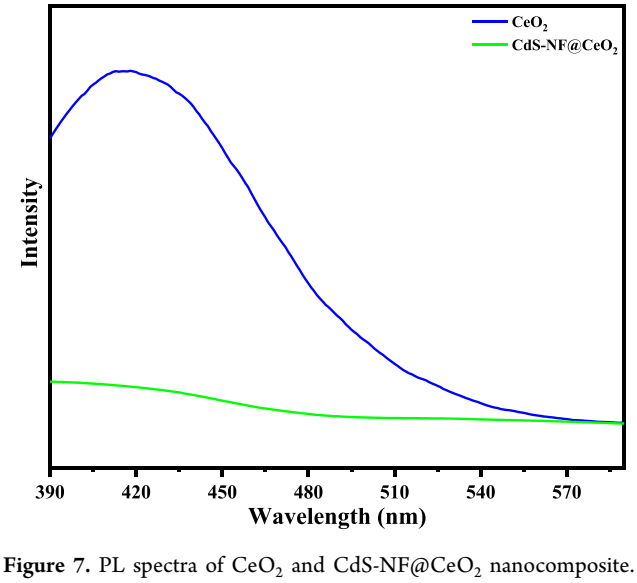

Figure 7. PL spectra of CeO_2 and CdS-NF@CeO_2 nanocomposite.

an excitation wavelength of 330 nm. It can be seen that bare CeO_2 has a very strong and wide peak at around 420 nm due to charge transfer between oxygen and cerium ions. However, the pronounced depression in the intensity of CdS-NF@CeO_2 confirmed the inhibition of photoinduced electron−hole pair recombination. Hence, the photogenerated electron and hole pairs could easily migrate between CdS and CeO_2 which results in superior photocatalytic efficiency of the CdS-NF@CeO_2 nanocomposite.

The photocatalytic activity of CdS@CeO_2 was evaluated by selecting CdS-NF@CeO_2 as the model catalyst due to its better characteristics as compared to the other morphologies.

3.2. FL Quenching of Cr(VI) in Water by the CdS-NF@CeO_2 Nanocomposite. The CdS-NF@CeO_2 aqueous suspensions (5 mg/mL) were used as the fluorescent probe. Upon introducing different concentrations of Cr(VI) to the catalyst suspension, Cr(VI) gets adsorbed onto the catalyst surface, which results in the quenching of FL intensity. This adsorption is supported by XRD findings in Figure S9 which clearly shows that all the peaks of the catalyst are intact but with decreased intensities. This decrease in intensities is due to the lowering of crystallinity or due to the filling of pores with Cr(VI) which weakens the scattering contrast. The quenching is clearly visible to the naked eye (Figure 8a). The FL intensity gets quenched proportionately upon increasing the Cr(VI) concentration. Furthermore, a calibration curve is plotted by using the Stern-Volmer relation for Cr(VI) concentrations from 0 to 0.5 μM (Figure 8b). A good linear correlation (R^2 = 0.9853) between $(F_0 - F)/F_0$ and Cr(VI) concentrations exist in the range of 0.05−0.5 μM (inset of Figure 8b) and the limit of detection,

$$\mathrm{LOD} = 3\sigma/S$$

where σ and S are the standard deviation of blank and slope of linearity, σ = 0.02 and, S = 1.49, respectively is calculated to be 0.04 μM. This limit is sufficiently lower than WHO's maximum permissible limit of 50 μg/L in drinking water. This suggests that the CdS-NF@CeO_2 is a highly efficient sensor and can be directly applied for Cr(VI) detection in aqueous media.

The same experiment was repeated under identical conditions by changing the catalysts for comparison. Figure 8c,d represents the FL titration curve for bare CdS-NF and CeO_2 catalysts, respectively. It can be concluded that although quenching is observed in both spectra, the CdS-NF@CeO_2 undergoes maximum quenching proportionately as compared to bare CdS-NF and CeO_2. Thus, the FL quenching ability was improved in the construction of the heterojunction between CdS-NF and CeO_2. The FL quenching percentage of Cr(VI) in CdS-NF@CeO_2 was calculated to be 94.6%.

The selectivity of the sensor toward Cr(VI) was evaluated by sensing various metal ions (Cr^{3+}, Hg^{2+}, Fe^{3+}, Cu^{2+}, Ni^{2+}, Pb^{2+}, Mn^{2+}, Ag^{+}, Al^{3+}, As^{5+}, Fe^{2+}, Au^{3+}, Zn^{2+}, and Co^{2+}) and anions (F^{-}, Cl^{-}, Br^{-}, I^{-}, CO_3^{2-}, PO_4^{3-}, SCN^{-}, SO_4^{2-}, and MnO_4^{-}) under identical conditions and procedure. Figure 9 shows that the cations and anions caused minimal FL intensity variation of the CdS-NF@CeO_2 nanocomposite, which establishes its promising sensing ability with superior selectivity toward Cr(VI).

The determination of Cr(VI) in tap water was carried out to validate the applicability of the proposed sensor in real samples. The tap-water and groundwater samples obtained from the Jorhat locality were spiked with 0.05, 0.25, and 0.5 μM Cr(VI) solutions under the optimized condition. As shown in Table 3, the calculated recoveries range from 99.8 to 107.0%. These results indicate that the proposed sensor is feasible and can be applied accurately for monitoring Cr(VI) in real water samples.

Table S2 summarizes a comparison between our sensor and other reported sensors. Evidently, this sensor possesses a

https://doi.org/10.1021/acsomega.2c05811
ACS Omega 2023, 8, 11768−11781

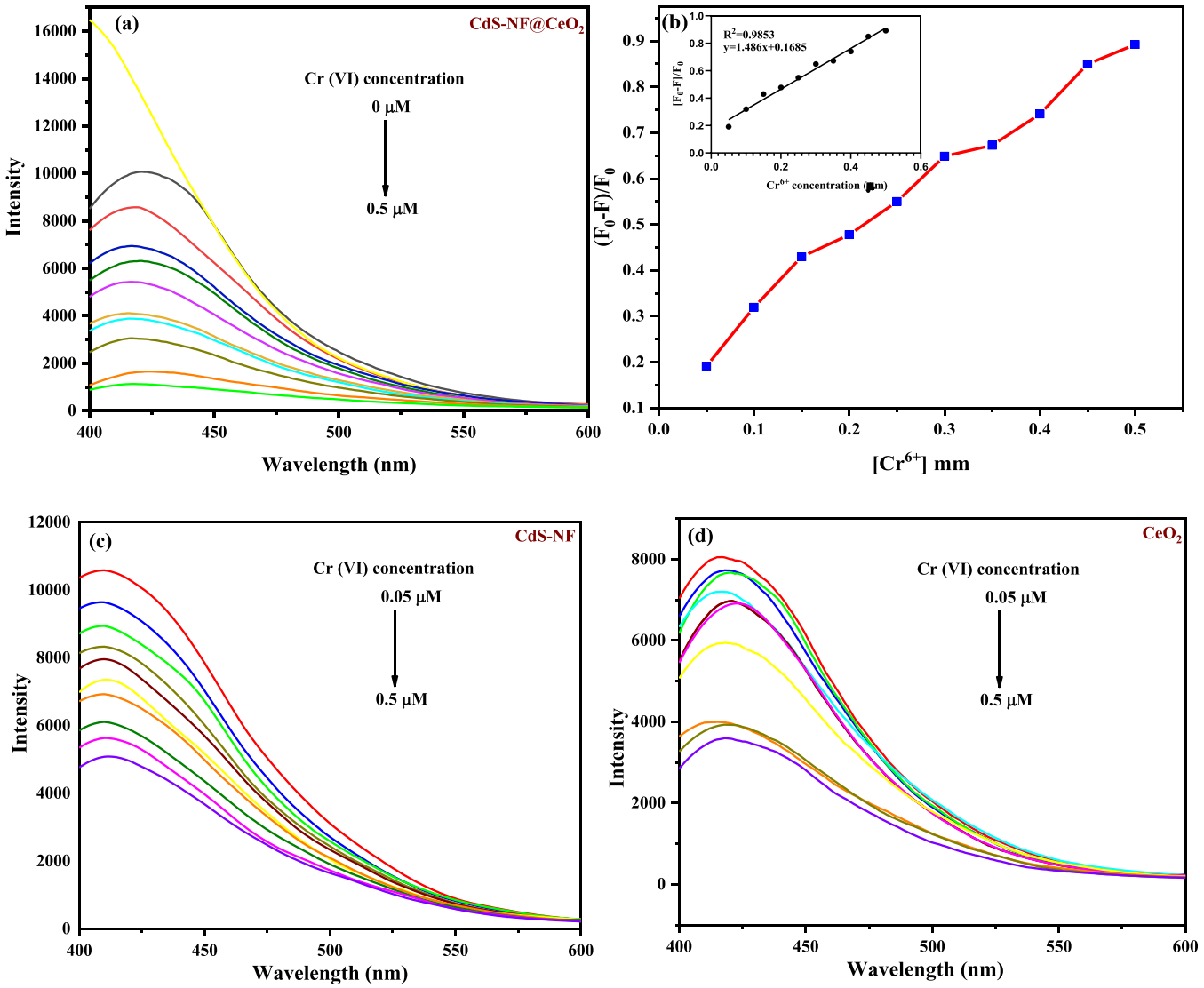

Figure 8. (a) FL titration spectra of CdS-NF@CeO_2 in the presence of varying concentrations of Cr(VI) (0−0.5 μm); (b) plot of $(F_0\text{-}F)/F$ against Cr(VI) concentration, the inset is the linear calibration plot for Cr(VI) detection; (c) FL titration spectra of CdS-NF in the presence of varying concentrations of Cr(VI) (0.05−0.5 μm); (d) FL titration spectra of CeO_2 in the presence of varying concentrations of Cr(VI) (0.05−0.5 μm).

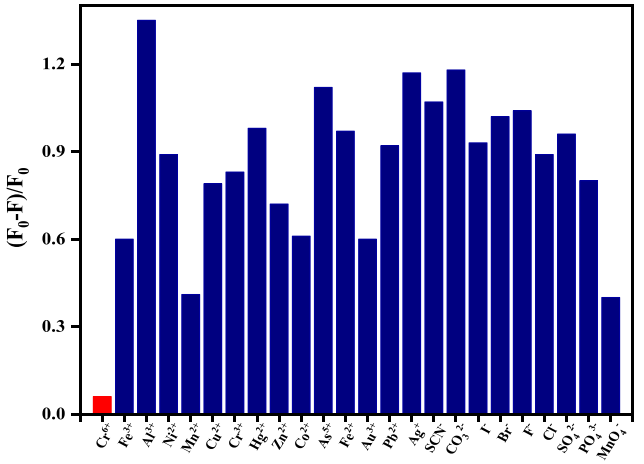

Figure 9. Selectivity of Cr(VI) based on $(F_0\text{-}F)/F_0$ in the presence of the CdS-NF@CeO_2 sensor.

Table 3. Concentration of Spiked Cr(VI) in the Tap Water Sample Analyzed by Using CdS-NF@CeO_2 as the Sensor (n = 3)

sample	spiked (μm)	found (μm)	recovery[n] (%)
tap water	0.1	0.105 ± 0.011	105.0
	0.2	0.214 ± 0.024	107.0
	0.3	0.310 ± 0.051	103.3
	0.4	0.399 ± 0.050	99.8
	0.5	0.501 ± 0.071	100.2

simple synthetic method, good linearity, and a relatively lower LOD value.

The quantum yield was calculated by the comparative method employing eq 1 and by using quinine sulfate as the reference standard.

$$\phi = \phi_R \times (I/I_R) \times (OD_R/OD) \times (\eta^2/\eta^2_R) \quad (1)$$

where ϕ, I, OD, and η represent the quantum yield, integrated intensity, optical density, and refractive index, respectively. The subscript R denotes the reference fluorophore (quinine sulfate)

https://doi.org/10.1021/acsomega.2c05811
ACS Omega 2023, 8, 11768−11781

of known quantum yield.Here, ϕ_R = 0.54, I_R = 824,644.00, I = 1,119,753.97, OD_R = OD = 0.05, η^2/η^2_R = 1.

Thus, the quantum yield was found to be 73%.

3.2.1. Mechanism of FL Quenching of Cr(VI). Three types of quenching are there viz. (a) static quenching, (b) dynamic quenching, and (c) inner filter effect (IFE). The FL quenching mechanism of CdS-NF@CEO_2 sensor was thoroughly studied. From the XRD spectra of CdS-NF@CeO_2 and Cr(VI) suspension (Figure S9), no change in 2θ can be seen after quencher (Cr(VI)) addition, which reveals the absence of generation of any new phase in the sensor, i.e., no Cr(VI) bonding interaction occurs with the CdS-NF@CeO_2 sensor and instead it gets well dispersed on to the pores of the sensor. The static quenching involves the formation of a non-fluorescent complex between the sensor (CdS-NS@CeO_2) and the quencher (Cr(VI)). Since, from the XRD study, no new phase formation was observed, thus the Cr(VI) quenching in our study does not involve the static mechanism.

When the excited state electron of the sensor returns to the ground state through energy or charge transfer between the quencher and the sensor, it is called dynamic quenching. In order to evaluate the dynamic mechanism, the FL lifetime of the sensor with and without the addition of quencher was measured. From Figure S10, in the FL lifetime measurements of the sensor (CdS-NF@CeO_2) with and without Cr(VI) addition, it can be seen that the lifetime remains constant at 4.64 ns, meaning that dynamic quenching is not the main quenching mechanism for this Cr(VI) sensing. Thus, IFE may be the main quenching mechanism.

IFE occurs when there is an overlap among the excitation or emission spectrum of the sensor with the absorption spectrum of the quencher. From Figure 10, it is clearly observed that a

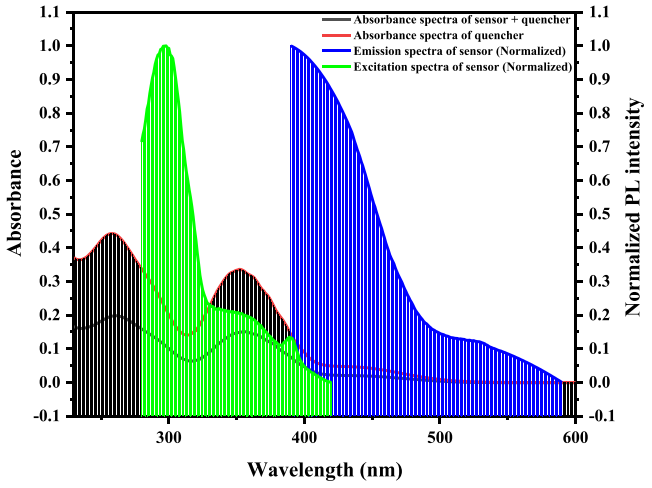

Figure 10. Mechanism of Cr(VI) quenching in the presence of the CdS-NF@CeO_2 sensor.

precise spectral overlap exists between the quencher's absorption band and the excitation and emission band of the sensor. Hence, the FL quenching mechanism of the CdS-NF@CeO_2-based sensor can be confirmed as the IFE, which accounts for the highly sensitive and fast response time of the CdS-NF@CeO_2 sensor.

3.3. Oxidative Coupling of Benzylamine to N-Benzylidenebenzylamine by CdS-NF@CeO_2 Nanocomposite with the Mechanistic Study. The photocatalytic activity of CdS-NF@CeO_2 was further investigated in the oxidative coupling of amine to imine by selecting benzylamine as the model substrate (Scheme 1). As shown in Scheme 1, the

Scheme 1. Oxidative Coupling of Benzylamine to N-Benzylidenebenzylamine

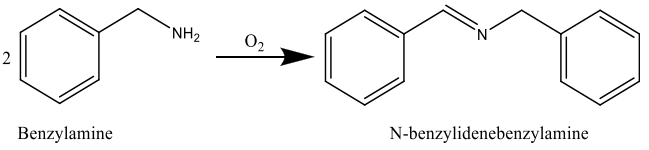

oxidative coupling of benzylamine (1 mmol) was carried out in the presence of CdS-NF@CeO_2 nanocomposites (10 mg), 1,4-dioxane (1.5 mL) and molecular oxygen under irradiation by four domestic LED bulbs (9 W each).

N-Benzylidenebenzylamine was obtained after 3 h of reaction under ambient conditions (Table 4, entry 1). However, in the absence of CdS-NF@CeO_2, benzylamine was hardly converted into the product, thus validating that the catalyst is mandatory for the reaction to proceed (Table 4, entry 2). Moreover, the reaction did not proceed in the absence of light substantiating that light is indispensable for the reaction and that the reaction is truly photocatalytic in nature (Table 4, entry 3). However, under natural light, 66.7% of benzylamine was converted to the desired product (Table 4, entry 4). Additional experiments were performed to investigate the mechanism of the reaction. When N_2 was purged into the system to eliminate the O_2, only a minimal amount of 16.2% benzylamine was converted to the product (Table 4, entry 5). Similarly, when O_2 was replaced by H_2O_2 and tert-Butyl hydroperoxide (TBHP) as oxidants, 38.1, and 86.6% conversions, respectively, were achieved. These results indicate that molecular oxygen is a pivotal part of the oxidative coupling reactions (Table 4, entries 6−7). Previous reports suggest that molecular O_2 accepts an excited electron from the HOMO of a photosensitizer and is converted to a superoxide radical.[5,42] To confirm the involvement of superoxide radicals in the reaction, p-benzoquinone was added as a superoxide scavenger to the reaction system (Table 4, entry 8). The substrate conversion markedly decreased to 8.6% which clearly specifies that superoxide formation is a crucial step in the reaction mechanism. The involvement of holes from the VB in oxidizing the benzylamine to yield a benzylamine radical cation was examined by adding triethanolamine as a hole scavenger (Table 4, entry 9). The pronounced decrease in benzylamine conversion verified the vital importance of holes in the reaction mechanism. Based on these findings, we propose a plausible reaction mechanism for the oxidative coupling of benzylamine to N-benzylidenebenzylamine (Scheme 2). From the XPS VB spectra, it was observed that the E_{VB} of CeO_2 (1.11 eV) is more positive than the E_{VB} of CdS (0.28 eV). On the other hand, the E_{CB} of CdS (−2.02 eV) is more negative than CeO_2 (−1.87 eV). Thus, on the illumination of the CdS-NF@CeO_2 nanocomposite, electrons from the VB get excited to the conduction band (CB), thus leaving holes in the VB. These excited electrons from the CB of CdS get transferred to the CB of CeO_2 and the holes from the VB of CeO_2 get transferred to the VB of CdS. In this way, the recombination of electron−hole pairs gets diminished and photocatalytic activity gets enhanced for the CdS-NF@CeO_2 nanocomposite. The reduction potential of O_2, $E(O_2/O_2^{\cdot-})$ = −0.33 eV, is less negative than the E_{CB} of CeO_2. As a result, the

https://doi.org/10.1021/acsomega.2c05811
ACS Omega 2023, 8, 11768−11781

Table 4. Oxidative[a] Coupling of Benzylamine to N-Benzylidenebenzylamine Using CdS-NF@CeO_2

entry	1	2	3	4[c]	5	6	7	8[d]	9[e]
CdS-NF@CeO_2	+	−	+	+	+	+	+	+	+
Hν	+	+	−	+	+	+	+	+	+
O_2	+	+	+	+	−	H_2O_2	TBHP	+	+
conversion[b] (%)	>99.9	2.3	0	66.7	16.2	38.1	86.6	8.6	0

[a]Reaction conditions: Benzylamine (1 mmol), CdS-NF@CeO_2 (10 mg), 3 h, 1,4-dioxane (1.5 mL), oxygen balloon. [b]Determined by GC. [c]In presence of natural light. [d]In presence of p-benzoquinone. [e]In presence of triethanolamine.

Scheme 2. Proposed Mechanism for the Oxidative Coupling of Benzylamine to N-Benzylidenebenzylamine

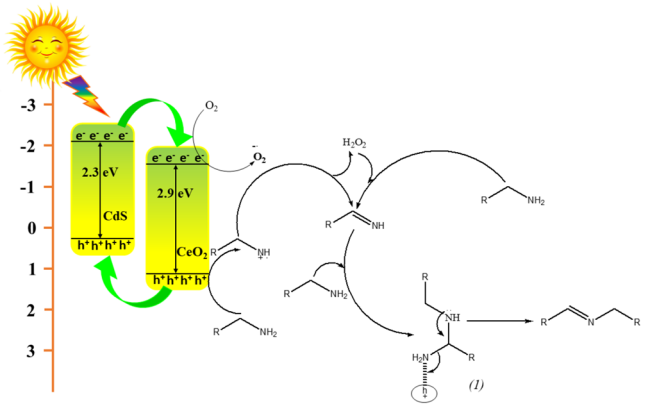

photoexcited electron from the CB of CeO_2 is accepted by the molecular O_2 to form a superoxide radical. In addition, the E_{VB} of CeO_2 is more positive than the oxidation potential of benzylamine (1.08 eV); hence the holes from CeO_2 are transferred to the primary amine, which yields intermediate amine radicals. Furthermore, Ph−CH═NH is generated by the reaction between the superoxide radical and intermediate amine radical. As no benzaldehyde was detected in our work, the Ph−CH═NH reacts with another benzylamine molecule to form the intermediate (1). Finally, the desired product is obtained by the hole-assisted elimination of the terminal amino group. However, extensive interpretation is still required for the complete exploration of this photocatalytic mechanism.

Next, several other reaction parameters were studied to evaluate the optimization of reaction conditions. After carrying out the reaction under optimized conditions in presence of the CdS@CeO_2 nanocomposites (Table 5, entries 1−5), it was observed that all the catalysts show high conversion and selectivity toward the benzylamine oxidations. When no solvent was added to the system, only 3.8% benzylamine was converted (Table 6, entry 1). Similarly, other organic solvents with different polarities, such as toluene, acetonitrile, tetrahydrofuran (THF), and cyclohexane, resulted in 6, 27, 16.2, and 20.6% conversion, respectively while 1,4-dioxane resulted in >99.9% conversion (Table 6, entries 2−6). In all cases, the selectivity was 100%. Thus, 1,4-dioxane was selected as the best solvent.

Table 5. Evaluation of Several Reaction Parameters for Photocatalytic Oxidative Coupling of Benzylamine to N-Benzylidenebenzylamine Using CdS-NF@CeO_2

entry	catalyst (10 mg)	conversion[a] (%)
1	CeO_2	75.6
2	CdS-HF@CeO_2	23.5
3	CdS-RL@CeO_2	98.7
4	CdS-S@CeO_2	92
5	10% CdS-NR@CeO_2	88

[a]Reaction conditions: Benzylamine (1 mmol); solvent (1.5 mL); oxygen balloon; time (3 h); room temperature.

Table 6. Evaluation of the Catalytic Activity of CdS@CeO_2 Nanocomposites for Photocatalytic Oxidative Coupling of Benzylamine to N-Benzylidenebenzylamine[a]

entry	solvent	oxidant	conversion[b] (%)	selectivity[c] (%)
1	no solvent	O_2	3.8	100
2	toluene	O_2	6	100
3	acetonitrile	O_2	27	100
4	THE	O_2	16.2	100
5	cyclohexane	O_2	20.6	100
6	1,4-dioxane	O_2	>99.9	100
7[d]	1,4-dioxane	O_2	100	100
8[e]	1,4-dioxane	O_2	2.4	100
9[f]	1,4-dioxane	O_2	4.9	100
10[g]	1,4-dioxane	O_2	100	100

[a]Reaction conditions: Benzylamine (1 mmol); CdS-NF@CeO_2 (10 mg); solvent (1.5 mL); oxygen balloon; time (3 h); room temperature. [b]Conversions were determined by GC peaks. [c]Selectivity to N-benzylidenebenzylamine. [d]0.5 mmol substrate. [e]2 mmol substrate. [f]5 mg catalyst. [g]15 mg catalyst.

Furthermore, when 0.5 and 2 mmol substrates were taken while keeping all other conditions unvaried, 100% conversion was obtained for 0.5 mmol whereas only 2.4% of 2 mmol substrates was converted (Table 6, entries 7−8). This suggests that on increasing the substrate amount there is a decrease in the available surface area of the catalyst for substrate adsorption. Similarly, the 5 mg catalyst resulted in a decrease (4.9%) in conversion due to the decrease in active sites provided by the catalyst (Table 6, entries 9−10). Table S3 summarizes a comparison between our catalyst and other reported catalysts, which shows that the catalytic activity of CdS-NF@CeO_2 for oxidative coupling of benzylamine to N-benzylidenebenzylamine is much better than the reported ones.

Thus, the CdS@CeO_2 nanocomposites possess superior photocatalytic activity and can be utilized for other photocatalytic applications.

3.3.1. Time Profile and Kinetics Study of Oxidative Coupling Reaction of Benzylamine to N-Benzylidenebenzylamine. The time-profile study was conducted for the oxidative coupling of benzylamine using CdS-NF@CeO_2 to evaluate the reaction kinetics (Figure 11). At 30 min intervals, an aliquot of the reaction mixture was drawn out, and the conversions were determined by GC analysis. Formation of N-benzylidenebenzylamine was observed during the course of the reaction and > 99.9 conversion was achieved at 3 h. Kinetic experiments revealed that the reaction is a first-order reaction with respect

https://doi.org/10.1021/acsomega.2c05811
ACS Omega 2023, 8, 11768−11781

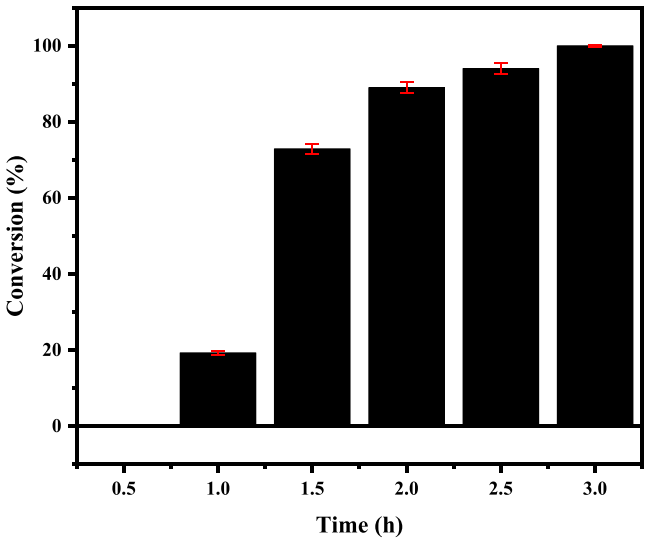

Figure 11. Time profile of the oxidative benzylamine coupling reaction by CdS-NF@CeO_2 catalyst. Reaction conditions: 1 mmol benzylamine, 10 mg CdS-NF@CeO_2, 1.5 mL 1,4-dioxane, 3 h, O_2 balloon. Error bars denote standard error.

to benzylamine having a rate constant of 3.33×10^{-4} s^{-1} (Figure 12).

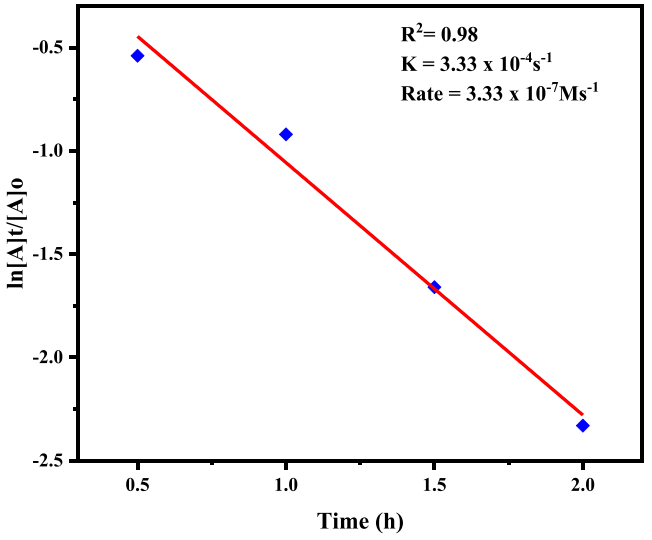

Figure 12. Kinetics plot of the oxidative benzylamine coupling reaction by CdS-NF@CeO_2 catalyst. Reaction conditions: 1 mmol benzylamine, 10 mg CdS-NF@CeO_2, 1.5 mL 1,4-dioxane, O_2 balloon. A_0, A_t denotes initial concentration and concentration at time t, respectively. K is the rate constant.

3.3.2. Recyclability. The most interesting property of a heterogeneous catalyst is its reusability. Figure 13 presents the recyclability graph of the CdS-NF@CeO_2 catalyst for 5 catalytic cycles of benzylamine oxidative coupling. It is evident from the graph that CdS-NF@CeO_2 is active even up to the fifth catalytic cycle giving a conversion of 98.3%.

4. CONCLUSIONS

In conclusion, several CdS morphologies loaded over the CeO_2 surface were synthesized by following a simple solvothermal route and were used as-synthesized. The CdS-NF@CeO_2 catalyst exhibits exorbitantly improved photocatalytic activity in the oxidative coupling of benzylamine to N-benzylidenebenzylamine via molecular oxygen as the oxidant with as high as >99.9% conversion and 100% selectivity. The versatility of the CdS-NF@CeO_2 catalyst was also corroborated by using it as a fluorescent sensor for the detection of Cr(VI) ions in water with a quantum yield of 73% and a LOD of 0.04 μM. This catalyst can be employed in a huge variety of photocatalytic C−N bond formation reactions and is also employed as an efficient sensor for the detection of metal ions with a very low detection limit.

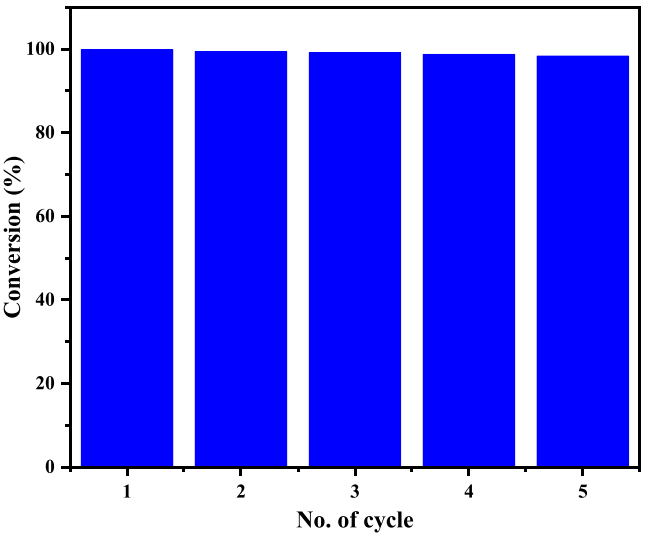

Figure 13. Recyclability test of the CdS-NF@CeO_2 catalyst.

■ ASSOCIATED CONTENT

Supporting Information

The Supporting Information is available free of charge at https://pubs.acs.org/doi/10.1021/acsomega.2c05811.

Materials and instrumentations, XRD spectra of recovered CdS-NF@CeO_2 nanocomposites, FTIR spectra of CdS-NF@CeO_2 nanocomposites, XPS spectra of CdS@CeO_2 nanocomposites, SEM image of CeO_2, SEM image of CdS-NF@CeO_2 after storing for 1 year under ambient conditions, EDS spectra of CdS-NF@CeO_2 nanocomposites, mapping analysis of CeO_2, absorbance spectra and Tauc plot of CdS@CeO_2 nanocomposites, XRD spectra of CdS-NF@CeO_2 and Cr(VI) suspension, comparison of surface areas of CdS-NF@CeO_2 with other reported CdS@CeO_2 nanocomposites, comparison of CdS-NF@CeO_2 for Cr^{6+} sensing with other reported catalysts, and comparison of CdS-NF@CeO_2 as a catalyst for oxidation coupling of benzylamine to N-benzylidenebenzylamine with reported catalysts (PDF)

■ AUTHOR INFORMATION

Corresponding Author

Lakshi Saikia − *Advanced Materials Group, Materials Sciences and Technology Division, CSIR-North East Institute of Science and Technology, Jorhat 785006 Assam, India; Academy of Scientific and Innovative Research (AcSIR), Ghaziabad 201002, India;* orcid.org/0000-0003-0892-7233; Phone: +91 376 2370 081; Email: lsaikia@neist.res.in, l.saikia@gmail.com; Fax: +91376 2370 011

https://doi.org/10.1021/acsomega.2c05811
ACS Omega 2023, 8, 11768−11781

Authors

Lisamoni Kalita − *Advanced Materials Group, Materials Sciences and Technology Division, CSIR-North East Institute of Science and Technology, Jorhat 785006 Assam, India; Academy of Scientific and Innovative Research (AcSIR), Ghaziabad 201002, India*

Karanika Sonowal − *Advanced Materials Group, Materials Sciences and Technology Division, CSIR-North East Institute of Science and Technology, Jorhat 785006 Assam, India; Academy of Scientific and Innovative Research (AcSIR), Ghaziabad 201002, India*

Purashri Basyach − *Advanced Materials Group, Materials Sciences and Technology Division, CSIR-North East Institute of Science and Technology, Jorhat 785006 Assam, India; Academy of Scientific and Innovative Research (AcSIR), Ghaziabad 201002, India*

Biswajit Saha − *Advanced Materials Group, Materials Sciences and Technology Division, CSIR-North East Institute of Science and Technology, Jorhat 785006 Assam, India; Academy of Scientific and Innovative Research (AcSIR), Ghaziabad 201002, India*

Complete contact information is available at: https://pubs.acs.org/10.1021/acsomega.2c05811

Notes

The authors declare no competing financial interest.

■ ACKNOWLEDGMENTS

The authors acknowledge the Director, CSIR-NEIST, Jorhat for his permission to publish this work. Lisamoni Kalita acknowledges DST, New Delhi for the INSPIRE fellowship grant.

■ REFERENCES

(1) Zhang, Y.; Tang, B.; Wu, Z.; Shi, H.; Zhang, Y.; Zhao, G. Glucose oxidation over ultrathin carbon-coated perovskite modified TiO_2 nanotube photonic crystals with high-efficiency electron generation and transfer for photoelectrocatalytic hydrogen production. *Green Chem.* **2016**, *18*, 2424−2434.

(2) Wang, C.; Astruc, D. Nanogold plasmonic photocatalysis for organic synthesis and clean energy conversion. *Chem. Soc. Rev.* **2014**, *43*, 7188−7216.

(3) Wu, Z.; Zhao, G.; Liu, J.; Zhang, Y.; Shi, H. A solar-driven photocatalytic fuel cell with dual photoelectrode for simultaneous wastewater treatment and hydrogen production. *J. Mater. Chem. A* **2015**, *3*, 3416−3424.

(4) Zhang, X.; Zhang, N.; Xu, Y.-J.; Tang, Z.-R. One-dimensional CdS nanowires−CeO_2 nanoparticles composites with boosted photocatalytic activity. *New J. Chem.* **2015**, *39*, 6756−6764.

(5) Bai, P.; Tong, X.; Wan, J.; Gao, Y.; Xue, S. Flower-like $Bi_2O_2CO_3$-mediated selective oxidative coupling processes of amines under visible light irradiation. *J. Catal.* **2019**, *374*, 257−265.

(6) Chen, J.; Cen, J.; Xu, X.; Li, X. The application of heterogeneous visible light photocatalysts in organic synthesis. *Catal. Sci. Technol.* **2016**, *6*, 349−362.

(7) Furukawa, S.; Ohno, Y.; Shishido, T.; Teramura, K.; Tanaka, T. Selective Amine Oxidation Using Nb_2O_5 Photocatalyst and O_2. *ACS Catal.* **2011**, *1*, 1150−1153.

(8) Yang, X.; Tao, H.; Leow, W. R.; Li, J.; Tan, Y.; Zhang, Y.; Zhang, T.; Chen, X.; Gao, S.; Cao, R. Oxygen-vacancies-engaged efficient carrier utilization for the photocatalytic coupling reaction. *J. Catal.* **2019**, *373*, 116−125.

(9) Liu, S.; Zhang, N.; Tang, Z.-R.; Xu, Y.-J. Synthesis of one-dimensional CdS@TiO_2 core-shell nanocomposites photocatalyst for selective redox: the dual role of TiO_2 shell. *ACS Appl. Mater. Interfaces* **2012**, *4*, 6378−6385.

(10) Li, X.; Hu, C.; Zhao, Z.; Zhang, K.; Liu, H. Three-dimensional CdS nanostructure for photoelectrochemical sensor. *Sens. Actuators, B* **2013**, *182*, 461−466.

(11) Zhai, T.; Fang, X.; Li, L.; Bando, Y.; Goldberg, D. One-dimensional CdS nanostructures: synthesis, properties, and applications. *Nanoscale* **2010**, *2*, 168−187.

(12) Wang, D.; Li, D.; Guo, L.; Fu, F.; Zhang, Z.; Wei, Q. Template-Free Hydrothermal Synthesis of Novel Three-Dimensional Dendritic CdS Nanoarchitectures. *J. Phys. Chem. C* **2009**, *113*, 5984−5990.

(13) Chen, M.; Kim, Y. N.; Li, C.; Cho, S. O. Controlled Synthesis of Hyperbranched Cadmium Sulfide Micro/Nanocrystals. *Cryst. Growth Des.* **2008**, *8*, 629−634.

(14) Wei, Z.; Kowalska, E.; Verrett, J.; Colbeau-Justin, C.; Remita, H.; Ohtani, B. Morphology-dependent photocatalytic activity of octahedral anatase particles prepared by ultrasonication−hydrothermal reaction of titanates. *Nanoscale* **2015**, *7*, 12392−12404.

(15) Jain, R.; Gopinath, C. S. Morphology-dependent, green, and selective catalytic styrene oxidation on Co_3O_4. *Dalton Trans.* **2019**, *48*, 4574−4581.

(16) Gu, S.; Chen, Y.; Yuan, X.; Wang, H.; Chen, X.; Liu, Y.; Jian, Q.; Wu, Z.; Zeng, G. Facile synthesis of CeO_2 nanoparticle sensitized CdS nanorod photocatalyst with improved visible-light photocatalytic degradation of rhodamine B. *RSC Adv.* **2015**, *5*, 79556−79564.

(17) Zhang, L.; Zhang, Y.; Guo, Y.; Wang, Y.; Liu, R.; Chen, B.; Zhong, H.; Zou, B. Growth of CdS nanotubes and their strong optical microcavity effects. *Nanoscale* **2019**, *11*, 5325−5329.

(18) Fang, Z.; Zhang, L.; Yang, T.; Su, L.; Chou, K.-C.; Hou, X. Cadmium sulfide with tunable morphologies: Preparation and visible-light driven photocatalytic performance. *Phys. E* **2017**, *93*, 116−123.

(19) Liu, S.; Yang, N.; Tang, Z.; Xu, Y. A nanotree-like CdS/ZnO nanocomposite with spatially branched hierarchical structure for photocatalytic fine-chemical synthesis. *Nanoscale* **2014**, *6*, 7193−7198.

(20) Shi, Y.; Chen, Y.; Tian, G.; Fu, H.; Pan, K.; Zhou, J.; Yan, H. One-pot controlled synthesis of sea-urchin shaped Bi_2S_3/CdS hierarchical heterostructures with excellent visible light photocatalytic activity. *Dalton Trans.* **2014**, *43*, 12396−12404.

(21) Yang, W.; Wu, W.; Chen, W.; Zhao, J.; Hu, X. Structural modulation of CdS/ZnO nanoheterojunction arrays for full solar water splitting and their related degradation mechanisms. *Catal. Sci. Technol.* **2018**, *8*, 5280−5287.

(22) Yang, Z.-M.; Huang, G.-F.; Huang, W.-Q.; Wei, J.-M.; Yang, X.-G.; Liu, Y.-Y.; Jiao, C.; Wan, Z.; Pan, A. Novel Ag_3PO_4/CeO_2 composite with high efficiency and stability for photocatalytic applications. *J. Mater. Chem. A* **2014**, *2*, 1750−1756.

(23) Ma, Y.; Bian, Y.; Liu, Y.; Zhu, A.; Wu, H.; Cui, H.; Chu, D.; Pan, J. Construction of Z-Scheme System for Enhanced Photocatalytic H_2 Evolution Based on CdS Quantum Dots/CeO_2 Nanorods Heterojunction. *ACS Sustainable Chem. Eng.* **2018**, *6*, 2552−2562.

(24) Arul, N.; Mangalraj, D.; Ramachandran, R.; Grace, A. N.; Han, J. I. Fabrication of CeO_2/Fe_2O_3 composite nanospindles for enhanced visible light driven photocatalysts and supercapacitor electrodes. *J. Mater. Chem. A* **2015**, *3*, 15248−15258.

(25) Zhang, N.-C.; Ouyang, T.; Chen, Y.; Wang, Z.; Chen, D.-Y.; Liu, Z.-Q. Ultrathin CdS shell-sensitized hollow S-doped CeO2 spheres for efficient visible-light photocatalysis. *Catal. Sci. Technol.* **2019**, *9*, 1357−1364.

(26) Mao, M.; Zhang, Q.; Yang, Y.; Li, Y.; Huang, H.; Jiang, Z.; Hu, Q.; Zhao, X. Solar-light-driven CO2 reduction by methane on Pt nanocrystals partially embedded in mesoporous CeO2 nanorods with high light-to-fuel efficiency. *Green Chem.* **2018**, *20*, 2857−2869.

(27) Barpuzary, D.; Qureshi, M. Enhanced Photovoltaic Performance of Semiconductor-Sensitized ZnO−CdS Coupled with Graphene Oxide as a Novel Photoactive Material. *ACS Appl. Mater. Interfaces* **2013**, *5*, 11673−11682.

(28) Wang, B.; Lin, Y.; Tan, H.; Luo, M.; Dai, S.; Lu, H.; Huang, Z. One-pot synthesis of N-doped carbon dots by pyrolyzing the gel

composed of ethanolamine and 1-carboxyethyl-3-methylimidazolium chloride and their selective fluorescence sensing for Cr(VI) ions. *Analyst* **2018**, *143*, 1906−1915.
(29) Gu, T.-Y.; Dai, M.; Young, D. J.; Ren, Z.-G.; Lang, J.-P. Luminescent Zn(II) Coordination Polymers for Highly Selective Sensing of Cr(III) and Cr(VI) in Water. *Inorg. Chem.* **2017**, *56*, 4668−4678.
(30) World Health Organization (WHO). *Chromium in Drinking-Water Background document for Development of WHO Guidelines for Drinking-Water Quality*; WHO: 1996.
(31) Biswas, S.; Dutta, B.; Mullick, K.; Kuo, C.-H.; Poyraz, A. S.; Suib, S. L. Aerobic Oxidation of Amines to Imines by Cesium-Promoted Mesoporous Manganese Oxide. *ACS Catal.* **2015**, *5*, 4394−4403.
(32) Jin, J.; Yang, C.; Zhang, B.; Deng, K. Selective oxidation of amines using O_2 catalyzed by cobalt thioporphyrazine under visible light. *J. Catal.* **2018**, *361*, 33−39.
(33) Kobayashi, S.; Mori, Y.; Fossey, J. S.; Salter, M. M. Catalytic Enantioselective Formation of C−C Bonds by Addition to Imines and Hydrazones: A Ten-Year Update. *Chem. Rev.* **2011**, *111*, 2626−2704.
(34) Mon, M.; Adam, R.; Ferrando-Soria, J.; Corma, A.; Armentano, D.; Pardo, E.; Leyva-Perez, A. Stabilized $Ru[(H_2O)_6]^{3+}$ in Confined Spaces (MOFs and Zeolites) Catalyzes the Imination of Primary Alcohols under Atmospheric Conditions with Wide Scope. *ACS Catal.* **2018**, *8*, 10401−10406.
(35) Yuan, H.; Yoo, W.-J.; Miyamura, H.; Kobayashi, S. Discovery of a Metalloenzyme-like Cooperative Catalytic System of Metal Nanoclusters and Catechol Derivatives for the Aerobic Oxidation of Amines. *J. Am. Chem. Soc.* **2012**, *134*, 13970−13973.
(36) Wu, S.; Sun, W.; Chen, J.; Zhao, J.; Cao, Q.; Fang, W.; Zhao, Q. Efficient imine synthesis from oxidative coupling of alcohols and amines under air atmosphere catalysed by Zn-doped Al_2O_3 supported Au nanoparticles. *J. Catal.* **2019**, *377*, 110−121.
(37) Huang, J.; Yu, L.; He, L.; Liu, Y.-M.; Cao, Y.; Fan, K.-N. Direct one-pot reductive imination of nitroarenes using aldehydes and carbon monoxide by titania supported gold nanoparticles at room temperature. *Green Chem.* **2011**, *13*, 2672−2677.
(38) Higashimoto, S.; Nakai, Y.; Azuma, M.; Takahashi, M.; Sakata, Y. One-pot synthesis of imine from benzyl alcohol and nitrobenzene on visible-light responsive CdS−TiO_2 photocatalysts. *RSC Adv.* **2014**, *4*, 37662−37668.
(39) Burrough, P.; Hamnett, A.; Orchard, A. F.; Thornton, G. Satellite structure in the X-ray photoelectron spectra of some binary and mixed oxides of lanthanum and cerium. *Dalton Trans.* **1976**, *17*, 1686−1698.
(40) Dong, W.; Pan, F.; Xu, L.; Zheng, M.; Sow, C. H.; Wu, K.; Xu, G. Q.; Chen, W. Facile synthesis of CdS@TiO_2 core−shell nanorods with controllable shell thickness and enhanced photocatalytic activity under visible light irradiation. *Appl. Surf. Sci.* **2015**, *349*, 279−286.
(41) Ganesh, R. S.; Sharma, S. K.; Durgadevi, E.; Navaneethan, M.; Binitha, H. S.; Ponnusamy, S.; Muthamizhchelvan, C.; Hayakawa, Y.; Kim, D. Y. Surfactant free synthesis of CdS nanospheres, micro-structural analysis, chemical bonding, optical properties and photo-catalytic activities. *Supperlattices Microstruct.* **2017**, *104*, 247−257.
(42) Lang, X.; Ji, H.; Chen, C.; Ma, W.; Zhao, J. Selective Formation of Imines by Aerobic Photocatalytic Oxidation of Amines on TiO_2. *Angew. Chem., Int. Ed.* **2011**, *50*, 3934−3937.

https://doi.org/10.1021/acsomega.2c05811
ACS Omega 2023, 8, 11768−11781